EBioMedicine 54 (2020) 102724

Contents lists available at ScienceDirect

EBioMedicine

journal homepage: www.elsevier.com/locate/ebiom

Research paper

Precise pulmonary scanning and reducing medical radiation exposure by developing a clinically applicable intelligent CT system: Toward improving patient care

Yang Wang[a,†], Xiaofan Lu[b,c,†], Yingwei Zhang[d,†], Xin Zhang[a], Kun Wang[a], Jiani Liu[a], Xin Li[a], Renfang Hu[e], Xiaolin Meng[e], Shidan Dou[e], Huayin Hao[e], Xiaofen Zhao[e], Wei Hu[e], Cheng Li[e], Yaozong Gao[e], Zhishun Wang[f], Guangming Lu[g], Fangrong Yan[b,c,*], Bing Zhang[a,**]

[a] Department of Radiology, The Affiliated Nanjing Drum Tower Hospital of Nanjing University Medical School, Nanjing 210008, PR China
[b] State Key Laboratory of Natural Medicines, China Pharmaceutical University, Nanjing, PR China
[c] Research Center of Biostatistics and Computational Pharmacy, China Pharmaceutical University, Nanjing 210009, PR China
[d] Department of Respiratory, The Affiliated Nanjing Drum Tower Hospital of Nanjing University Medical School, Nanjing 210008, PR China
[e] Department of Research Center of CT BU, Shanghai United Imaging Healthcare Co., Ltd., 2258 Chengbei Rd., Jiading District, Shanghai 201800, PR China
[f] Department of Psychiatry and Translational Imaging, Vagelos College of Physicians and Surgeons, Columbia University, New York 10032, United States
[g] Department of Medical Imaging, Jinling Hospital, School of Medicine, Nanjing University, Nanjing 210002, PR China

ARTICLE INFO

Article History:
Received 13 January 2020
Revised 21 February 2020
Accepted 4 March 2020
Available online xxx

Keywords:
Artificial intelligence
Computed tomography
Automatic pulmonary scanning
Interstitial lung disease
Radiation exposure

ABSTRACT

Background: Interstitial lung disease requires frequent re-examination, which directly causes excessive cumulative radiation exposure. To date, AI has not been applied to CT for enhancing clinical care; thus, we hypothesize AI may empower CT with intelligence to realize automatic and accurate pulmonary scanning, thus dramatically decrease medical radiation exposure without compromising patient care.
Methods: Facial boundary detection was realized by recognizing adjacent jaw position through training and testing a region proposal network (RPN) on 76,882 human faces using a preinstalled 2-dimensional camera; the lung-fields was then segmented by V-Net on another training set with 314 subjects and calculated the moving distance of the scanning couch based on a pre-generated calibration table. A multi-cohort study, including 1,186 patients was used for validation and radiation dose quantification under three clinical scenarios.
Findings: A U-HAPPY (United imaging Human Automatic Planbox for PulmonarY) scanning CT was designed. Error distance of RPN was 4·46±0·02 pixels with a success rate of 98·7% in training set and 2·23±0·10 pixels with 100% success rate in testing set. Average Dice's coefficient was 0·99 in training set and 0·96 in testing set. A calibration table with 1,344,000 matches was generated to support the linkage between camera and scanner. This real-time automation makes an accurate plan-box to cover exact location and area needed to scan, thus reducing amounts of radiation exposures significantly (all, $P<0·001$).
Interpretation: U-HAPPY CT designed for pulmonary imaging acquisition standardization is promising for reducing patient risk and optimizing public health expenditures.
Funding: The National Natural Science Foundation of China.

1. Introduction

Interstitial lung disease (ILD) requires the highest frequency of re-examination, which directly causes a side effect of excessive cumulative radiation exposure for patients [1], and incidence of lung cancer among patients with ILD was high. Low-dose computed tomography (CT) is the only recommended test for the follow-up such disease. Since its introduction in the 1970s, computed tomography (CT) has revolutionized diagnostic decision-making [2]. Recent years have witnessed a remarkable transformation of several generations of CT, which are all pursuing faster and better imaging methods [3]. Low-dose chest CT screening has become one of the most effective means for early-stage lung cancer screening recognized worldwide [4-6]. Almost all clinicians, imaging scientists, radiologists, and physicists worldwide desire the lowest radiation dose for patients, as

* Corresponding author at: Research Center of Biostatistics and Computational Pharmacy, China Pharmaceutical University, No. 639 Longmian Avenue, Nanjing 210009, PR China.
** Corresponding author.
E-mail addresses: f.r.yan@163.com (F. Yan), zhangbing_nanjing@nju.edu.cn (B. Zhang).
† These authors contributed equally.

https://doi.org/10.1016/j.ebiom.2020.102724

Research in context

Evidence before this study

We searched PubMed for publications on artificial intelligence-navigated automatic pulmonary scanning systems published from database inception to Aug 31, 2018, using search terms "artificial intelligent" or "AI", "computerized tomography" or "CT" or "CT scanning", "pulmonary" or "lung" or "chest", and "image acquisition" without language restrictions. The results of the scientific literature search were limited. Until now, artificial intelligence has not been experimented with the enhancement of the upstream clinical care, especially imaging acquisition.

Added value of this study

We developed a U-HAPPY (United imaging Human Automatic Planbox for PulmonarY) scanning CT, an intelligent system capable of automating chest, based on 76,882 human faces for facial detection, 377 subjects for pulmonary segmentation and 1186 patients for independent validation. Through multi-center verification, U-HAPPY CT makes an accurate planbox to cover exact location and area that needs to scan, which thus reduces amounts of radiation exposures significantly in clinical scenario that fully navigated by this real-time automation system as compared to other scenarios with either semi-navigation or pure manual.

Implications of all the available evidence

To the best of our knowledge, U-HAPPY CT is the first AI-navigated system that is clinically applicable for automate pulmonary scanning, which maintained a robust scanning performance but dramatically decreased the manual operation of radiographers, optimizing the efficiency of diagnosis, reducing the radiation exposures, and thus improving the patient care. It is anticipated that the scanning technology we propose here will become a powerful tool for optimizing the whole clinical workflow and will be both extended to scanning other body parts and deployed to other imaging methods (e.g., X-ray and MRI). We believe that by incorporating such a novel concept, a new standard for intelligent CT examination in the future could be established and achieve more standard images for future AI-related medical studies.

well as the highest quality medical images and most accurate imaging approaches [7,8]. Obviously, significant improvement has been made for image quality, but low-dose scanning methods remain unexplored.

To avoid incomplete scanning, radiographers expand the scanning range, which inevitably leads to unnecessary radiation exposure. Thus far, all aspects of CT operation require the manual involvement of radiographers, which not only results in additional exposure but is also costly. The irregularity of manual operation also leads to the arbitrary and casual determination of scan protocol parameters [9]; thus, a critical unmet need is the elimination of the human error to optimize the clinical image workflow.

The desire to improve the efficacy and efficiency of clinical care continues to drive multiple innovations into practice, including artificial intelligence (AI). With the ever-increasing demand for health care services and the considerable drain on human resources, AI has infiltrated the optimization and streamlining of clinical workflows [10-14] but remains unexplored inmost upstream medical data collection processes [15]. Therefore, we hypothesize that AI may empower CT with intelligence, thereby decreasing the manual operation of radiographers, improving the efficiency of imaging diagnosis, and reducing the radiation dose. To this end, the U-HAPPY (United imaging Human Automatic Planbox for PulmonarY) scanning CT was born, which indicates for the first time that a new generation of intelligent CT concept has been proposed.

2. Methods

2.1. Study design and participants

Since the imaging approach of ILD during follow-up is not different from other lung diseases, no special exclusion criteria set for enrolment of patients with potential pulmonary lesions. All CT scanning imaging was performed as routine clinical care for patients, all scans were downloaded as DICOM format (Table S1), and no exclusion criteria of age or gender were involved. Another dataset comprised of 1186 patients was used for independent testing, among which 558 cases were collected for retrospective study and 628 cases were enrolled for prospective validation (see more details in Supplementary Materials). All images that comprised the testing dataset were randomly collected from five hospitals, and patients involved in this dataset underwent a routine baseline or contrast-enhanced chest CT between July 2018 and Sep 2019. No special exclusions were included (see more details of the independent cohort in Table 1). Prospective validation was applied to newly admitted patients, including 473 admitted by our institution (Nanjing Drum Tower Hospital) and 155 admitted by other hospitals (Pizhou Third People's Hospital [n = 87]; Chenyang Health Center in the Sheyang District [n = 68]). A total of 558 retrospective cases were used for independent validation. An independent testing cohort was divided into three parts: a) the united imaging (UI) group derived from Nanjing Drum Tower Hospital (n = 351), which was fully equipped with a U-HAPPY CT and involved no manual operation; b) the manual but U-HAPPY CT-adjusted group from three hospitals: Nanjing Drum Tower Hospital (n = 122), Pizhou Third People's Hospital (n = 87), and Chenyang Health Center in the Sheyang District (n = 68); c) the chest CT scanning group in which the scans were entirely operated manually without any assistance of U-HAPPY CT, which also consisted of three hospitals: Nanjing Drum Tower Hospital (n = 321), Jiangsu Provincial Hospital (117) and Gaochun People's Hospital (n = 120). All the collected CT images were acquired by multi-

Table 1
Characteristics of objects used in this study.

Parameters	Objects (images) metric*
Facial detection	
Number of objects (training/validation datasets)	76,382/500
Lung field segmentation	
Number of objects (training/validation datasets)	314/63
Ratio of female to male	0·80:1 (140:174)/0·75:1 (27:36)
Age (years)	56·0 ± 0·8/57·4 ± 1·6
Camera couch calibration	
Number of positions (sparse sampling/calibration)	80/1344,000
Independent testing in multi-cohorts	
Number of patients (independent testing datasets)	1186
Ratio of female to male	0·77:1 (517:669)
Age (years)	57·1 ± 0·5
Median total length of the lung (range, mm)	311·07 ± 1·19
Median actual length of the lung (range, mm)	265·78 ± 1·02
Different manufacturers	Number of patients
United Imaging	738
GE	101
Philips	110
Siemens	117
Toshiba	120

* Continuous value was presented with mean ± standard error of the mean.

detector row CT scanners (GE; Philips, Siemens; Toshiba; and United Imaging) with a specific radiation protocol (see more details of the acquisition and reconstruction parameters in Supplementary Table S1). The dataset corresponding to such validation was further stored in a picture archiving and communication system (PACS) to compare scanning performance among different hospitals. All images were reviewed independently by two radiologists (J. L, three years of experience; Y. W, 11 years of experience). We designed an evaluation framework to assess the accuracy of U-HAPPY CT. Specifically, each of the four boundaries (left, right, apex, and basis) was evaluated separately by calculating the distance between the boundary and the gold standard. The smaller the distance was, the more accurate the positioning was. To facilitate this evaluation framework, we empirically classified the distance error into two categories, i.e., success or failure. All patients were not subjects recruited for studying U-HAPPY CT, but ordinary patients who were routinely admitted to the hospital and need to undergo CT scans. This study was approved by the ethics commissions of the five hospitals, with a waiver of informed consent. This work was conducted in a manner compliant with the People's Republic of China Health Insurance Portability and Accountability Act and was adherent to the tenets of the Declaration of Helsinki.

2.2. Image labeling

Before training, each image was labeled by two senior independent imaging experts, each with over ten years of clinical imaging experience. First, each image went through a labeling system, and the lung field boundary was labeled by one expert who conducted quality control and excluded chest CT images containing severe artefacts or significant image resolution reductions. Second, another expert verified the true labels for each image and arbitrated disagreements in clinical labels to account for human error in labeling.

2.3. Installation of the camera

According to the technical parameters provided by the camera manufacturer (Hikvision Digital Technology Co., Ltd, Hangzhou) and the actual test results, a camera installation range relative to the fixed position of the scanning couch is given. If the ceiling position is within the installation space of the camera, the camera is directly mounted on the ceiling; if the ceiling is too high or too low or if there are other conditions such as air conditioners or lamps that do not meet the installation requirements, the solution is mainly to add a bracket that can be used to support the camera installation. After the installation is completed, the angle of the camera needs to be adjusted so that the scanning couch is at the center of the field of view and is substantially parallel to the lateral edges of the camera. Therefore, the relative position between the camera, the scanning couch and the gantry is fixed (Fig. 1).

2.4. Model architecture of region proposal network (RPN) and V-Net

To locate the starting line of pulmonary topograms, we harnessed RPN [16] to realize facial detection and specified the jaw's outer edge as the scanning starting line (see more details in Fig. 2a and Data sharing section). Specifically, we trained and selected the final model based on a public database (i.e., WIDERFace http://mmlab.ie.cuhk.edu.hk/projects/WIDERFace) with 12,862 images, including 76,382 human faces with provided position as gold standard. The final model was further tested on 500 images collected by a camera assembled on the ceiling related to the United Imaging Healthcare CT device. Gold standard used for testing was labeled by two experts (C.Q., 17 years of experience; X.W., 11 years of experience). The training set was directly input into RPN with 170,000 epochs of training, and the loss of border regression took a smooth-L1 as loss function to evaluate the training and testing performance. The smooth-L1 can be formulized as follows:

$$smooth_{L_1}(x) = \begin{cases} 0.5x^2, & if\ |x| < 1 \\ |x| - 0.5, & otherwise \end{cases}$$

We applied V-Net to segment the pulmonary area on topograms and determine the area boundaries. We empirically adjusted the boundaries to obtain the 'scanning planbox' that was originally fully determined manually. Specifically, the pulmonary topogram dataset included 314 topograms of training data and 63 of testing data obtained between April 2015 and May 2017 (see parameter details in Table S2). The left and right lung areas in the topograms were labeled by two senior radiologists as gold standard (C.Q.; X.W.). The source code of V-Net was modified to realize multi-label segmentation on 2-dimensional data, including two main points: 1) the network input and gold standard were transformed into 2-dimensional form, and size of the image was fixed as a 512 × 512 matrix; 2) the output was amended to three channels in the last convolutional layer, representing the left lung, right lung and background (Fig. 2a; see the Data sharing section for more details). To enhance robustness, random translation and rotation of the original data were performed in the training process to simulate a series of image scenes encountered in a practical clinical environment to add incremental training to the training set. During the training process, the data were pre-processed and normalized with a uniform size of 512 × 512. The normalized data were further input into V-Net for end-to-end training with 300,000 epochs. We utilized the Dice's coefficient as a loss function to evaluate the training and testing performance. The Dice's coefficient can be formulized as follows:

$$Dice's\ coefficient = \frac{2\sum_i^N p_i g_i}{\sum_i^N p_i^2 + \sum_i^N g_i^2}$$

We denoted the total number of pixels that needed to be traversed as N, the predicted segmentation region as $\{p_i | p_i \in P\}$, and the gold standard segmentation region as $\{g_i | g_i \in G\}$ (see experimental software and hardware required to train the network in Supplementary Materials).

2.5. Camera and CT scanning couch calibration process

To enable the CT scanning couch to automatically move the target's starting position to ISOcentre under the camera navigation (Fig. 3a), a calibration table was generated as a linkage between the two devices; this process was simplified to a 3-point plus 3-line calibration (Fig. 3a), and the couch movement was simplified into horizontal and vertical directions. We adopted concise white bar pattern recognition, sparse sampling and fitting to obtain the relationship between the couch and the camera pixel (see more details in Supplementary Materials).

2.6. Quantification of effective radiation dose

To quantify the extent of the dose reduction when applying U-HAPPY CT, we calculated the effective dose per patient based on the formula $mSv = DLP \times C_f$, where dose length product (DLP) is a measure of CT tube radiation output/exposure, and C_f was set as 0·014 as the conversion factor for chest CT [8, 17, 18]. The absolute mSv value per patient was further scaled as $mSv_{\%}$ to eliminate the effect of different scanning protocols selected by different hospitals.

2.7. Experimental software and hardware

All network models were trained on the DGX platform (NVIDIA DGX system, 4X Tesla V100 GPUs, 128 GB total system GPU Memory,

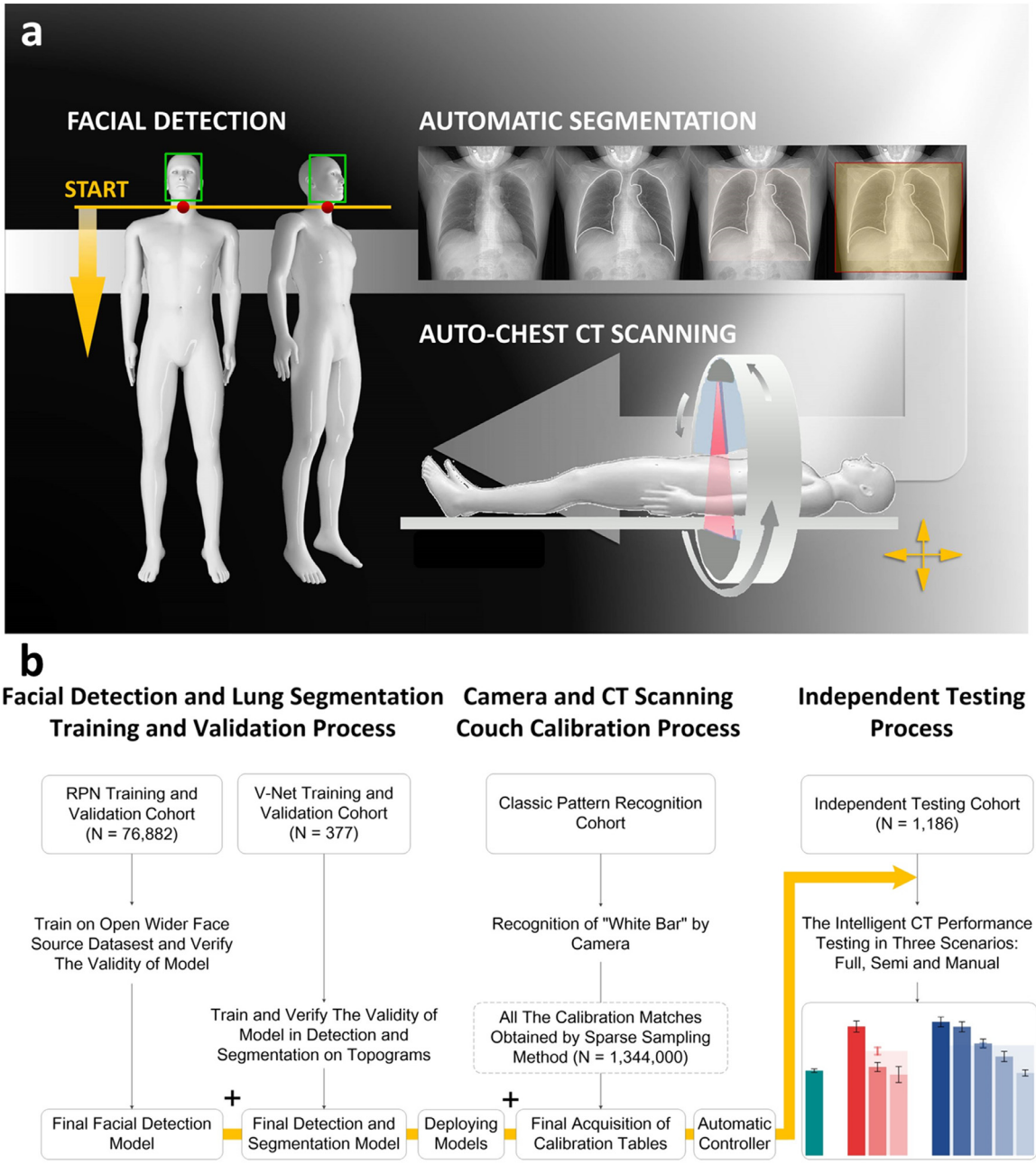

Fig. 1. The technical framework of U-HAPPY CT implementation and the entire workflow for each respective dataset. a) First, facial detection (green rectangle) and determination of the starting position of the CT scanning of the thorax (red point) were performed. Second, automatic segmentation of the lung field can be disassembled into four steps: i) acquisition of the chest topogram by scanning with a fixed empirical scanning length of 400 mm; ii) automatic segmentation of the lung field by applying the V-Net algorithm; iii) determination of the lung field boundaries by marking a transparent light gray rectangular box; and iv) determination of the thorax range boundaries by marking a red rectangular box with empirical complementary lengths of 20, 50, 40 and 40 mm for lung apex, basis, left side and right side. Third, auto-chest CT scanning depends on the linkage of the former two steps, with CT couch motion split into two directions during the thoracic CT scanning process. These three parts were connected, along with the gray arrow, to progress. b) Our work was designed in three parts where the first part included concatenating two convolutional neural networks (RPN and V-Net), which were utilized for facial boundary detection and lung field segmentation of topograms. The second part consisted of classic pattern recognition and calibration table generation, and in the third part, we deployed the final model to multi-center cohorts to evaluate the model performance. (For interpretation of the references to color in this figure legend, the reader is referred to the web version of this article.)

dual 20-core Intel Xeon E5-2698 CPU v4 2.2 GHz, Santa Clara, California, USA). All network models were trained using the PyTorch framework with PyTorch 1.1.0. Python 2.7.16, and CUDA 10.0. The trained neural networks were run on the CT scanner host in different independent hospitals. The software version was R001 (Shanghai United Imaging Healthcare Co., Ltd., Shanghai, China), in which Gantry Software and Console Software were run on Debian Linux 8.0 64-bit Edition and Windows 7, respectively. The hardware platforms were an Intel (R) Core (TM) i3 4 GHz and Intel (R) Xeon e5-1620 v4 (Intel, Santa Clara, CA, USA), respectively.

2.8. Statistical analyses

Continuous variables were described as the mean ± standard error of the mean (SEM). The differentiations were compared between two groups using a two-sample Student's *t*-test. Multiple group comparisons were followed by one-way ANOVA. Kappa statistics and Bland-Altman (BA) plot were used to measure the degree of consistency between two appraisers; the differences are plotted versus the average of two appraisers in BA plot and the corresponding statistical *P* value was calculated for testing a constant difference

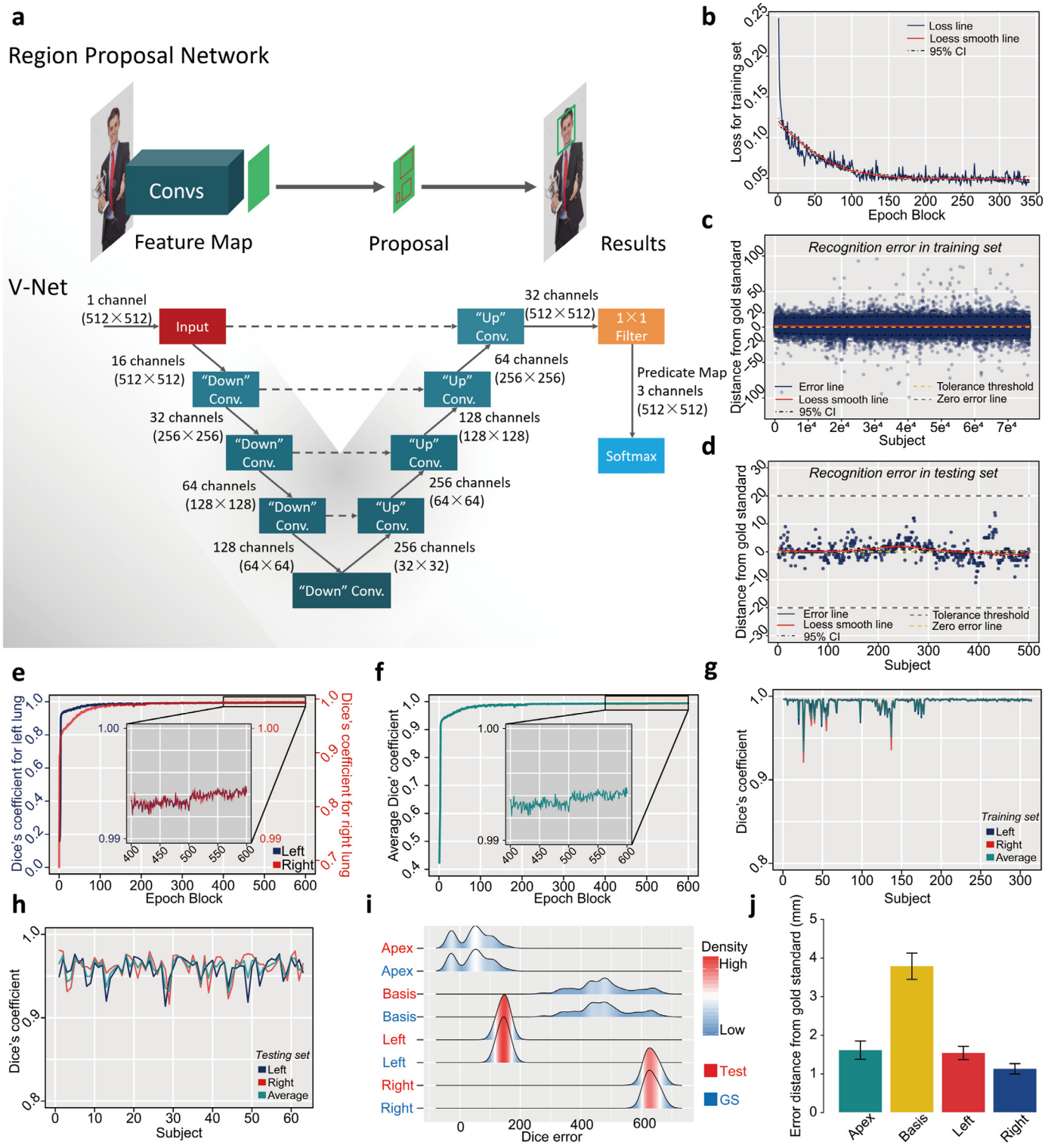

Fig. 2. Schematic representation of the applied network architecture, the training process of the RPN and model evaluation via the testing set and the pulmonary segmentation Dice's coefficient measurement in both the training and testing procedures. a) The networks include both the RPN used for locating the scanning the starting position and the V-Net used for pulmonary field segmentation. b) The loss curve of the training process converges and tends to 0 after 340 epoch blocks (340 × 500 epochs). The errors derived from the training and testing procedure are shown in c) and d), respectively, where the vast majority of errors were located in the tolerance interval of ±20 pixels for the training procedure and all errors were tolerable in the verifying procedure. The solid blue line represents the true loss or error, and the red line represents the corresponding loss smooth curve with a 95% confidence interval, shown as a dashed black line. Pulmonary segmentation Dice's coefficient measurement in both the training and testing procedures is shown in e-h. e) With the increase in epoch blocks (1 epoch block equals to 500 epochs, a total of 300,000 iteration epochs in the training set including 314 topograms), the Dice's coefficient increases rapidly and approaches the peak value of 1. The Dice's coefficients of the left and right lungs converge and approach 1 in the tailing 400–600 epoch blocks of the training procedure. The averaged Dice's coefficient for the left and right lungs is shown in f). The exact Dice's coefficient curves by deploying the model to both the training set and the testing set for the left and right lungs and the average set are shown in g) and h), respectively. i) Consistency between the V-Net derived segmentation and the gold standard is presented with a ridge plot and kappa statistic; GS: gold standard. j) Absolute errors in four boundaries are presented as the mean±standard error of the mean. (For interpretation of the references to color in this figure legend, the reader is referred to the web version of this article.)

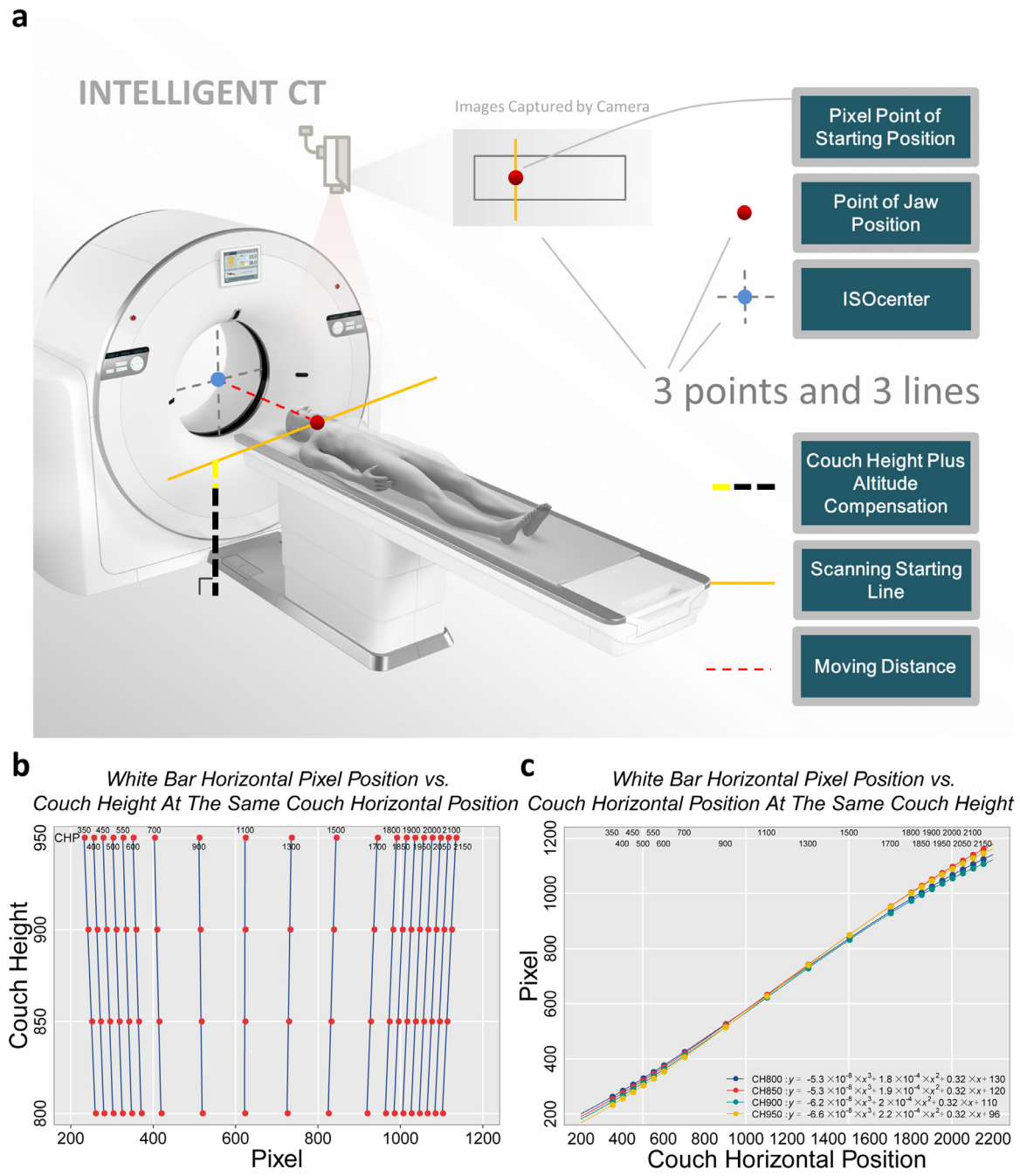

Fig. 3. The schematic representation of the principle of calibration used in the study and the corresponding relationship between the pixel position and couch height as well as the couch code with the white bar as the correction object. a) The basic principle and key factors (3-points and 3-lines) of the U-HAPPY CT scanning couch automatic positioning. This diagram included key factors associated with both the CT scanner and the 2-dimensional camera. A key point related to the camera was the pixel position point imaged inside the camera where the key starting position point in the camera detection process is located. This point corresponds to the orange-yellow position (the red dot on the solid orange line) where the subject starts at the CT scan couch, which is also a critical part of the scanner: Since the protocol was selected, the CT scan couch automatically obtained a fixed couch height and altitude compensation (black dotted lines superimposed with yellow dashed lines). Since the position of the ISOcentre (gray dotted cross), the pixel points of the starting position and the height of the scanning couch are known, the displacement distance of the scanning couch (red dotted line) can be obtained by looking up the calibration table. b) Linear relationship between the horizontal pixel position of the white bar and the couch height under the same couch code. c) Nonlinear relationship between the horizontal pixel position of the white bar and the couch code at the same couch height. CHP, couch horizontal height. (For interpretation of the references to color in this figure legend, the reader is referred to the web version of this article.)

based on a null hypothesis—the slope equals to 0 in the linear regression of differences on averages. Critical difference was also provided in BA plot, i.e., 'two' times standard deviation of differences, equals half the difference of lower and upper limit. For all statistical analyses, a two-tailed *P* value <0·05 was considered statistically significant and was conducted by R (version 3.6.2).

3. Results

3.1. Facial detection performance

The technical skelecton of U-HAPPY CT was delineated in Fig. 2a. After 170,000 epochs (500 epochs for each epoch block) of the RPN,

the loss curve converged to approximately zero (Fig. 2b). Since facial detection here was not a binary classification, no sensitivity or specificity could be measured. Therefore, we reasoned that all the detection falling within a tolerance interval was successful, and the model validity was evaluated based on the success rate. We assumed that a less than 20 pixels (approximately 5.3 mm) error distance from the gold standard was clinically tolerable. The model was first tested on the training set that contained 76,382 human faces, and the error distance ranged from −99 to 96 pixels (4·46± 0·02 pixels for absolute error), with a success rate of 98·7% (75,374/ 76,382) (Fig. 2c). Furthermore, we verified that the error distance of the testing set that contained 500 human faces ranged from −11 to 14 pixels (2·23±0·10 pixels for absolute error), and the success rate was 100% (Fig. 2d). Considering that the success rate regarding the testing set was more favorable than the training set, overfitting was addressed properly.

3.2. Segmentation performance

We found that within 300,000 epochs of iteration, Dice's coefficient rapidly increased and tended to be stable and convergent to the peak value of one, regardless of the training procedure of the left or right lung (Fig. 2e). Dice's coefficient for training ranged from 0·159 to 0·995 for the left lung and from 0·687 to 0·995 for the right lung. In the tail 400−600 epoch blocks, the average Dice's coefficient of bilateral lungs reached a mean value of 0·994 (Fig. 2f). Final model derived from the training procedure was further deployed on the training set and an independent testing set including 63 topograms; we found that the average Dice's coefficient ranged from 0·93 to 1·00 (0·99±0·0004; Fig. 2g) in the training set and from 0·93 to 0·98 (0·96±0·001; Fig. 2h) in the testing set, indicating an accurate pulmonary segmentation due to all coefficients greater than 0·9. We further measured the position of the plan-box in the testing set and compared it with gold standard; we found in all boundaries, the V-Net-derived segmentation shared significant consistency with the gold standard (all; kappa>0·98, $P<0·0001$; Fig. 2i). Additionally, BA plots revealed significant consistency between the measurement in testing set and gold standard in terms of four pulmonary boundaries (all slope tests; $P>0·05$; Fig. S1). Each boundary presented with a tolerable absolute error within 10 mm, and a relatively high error existed in the measurement of the basis compared to those of other boundaries (Apex: 1·61±0·24 mm; Basis: 3·78±0·34 mm; Left: 1·53± 0·17 mm; Right: 1·12±0·13 mm; Fig. 2j), which may be due to an anatomical confounding factor formed by the junction between air and soft tissue mixed with bone structure.

3.3. The generation of camera-CT scanning couch calibration table

Utilizing specific physical position of the subject that needs to be scanned and the size of the required scanning range, we linked each pixel position of the camera to the physical position of the CT scanning couch one by one. We decomposed the scanning couch into two parts (Fig. 3a), one of which was the relationship between the pixel position and different couch heights under the same couch code. We found that this relationship was almost a perfectly linear fit ($Pixel = k \times Couch\ Height + b$; Fig. 3b; Table S3). Additionally, we reasoned that under the same couch height, the nonlinear relationship between the horizontal pixel position of the white bars and the couch code can be covered by spline interpolation (Fig. 3c). When partial data were collected, we used sparse sampling to calculate the corresponding pixel position within the effective operating space range of the entire CT scanning couch (all couch heights and sizes) to obtain a final calibration table with 1344,000 matches (see more details in the section of Data sharing).

3.4. Independent multi-cohorts testing and reduction in radiation dose

Three scenarios were adopted for independent multi-cohorts testing, that is, full- and semi-navigation of U-HAPPY CT and one scenario completely operated manually. To visually display the difference in image acquisition under two extreme scenarios (i.e., full and manual), we selected two cases diagnosed with ILD that required long-term CT follow-up. Specifically, the two patients received CT scanning for image acquisition under the full and manual scenarios; image reconstruction and the corresponding top and bottom slices were shown in Fig. 4a−h. Dramatically more unnecessary scanning region could be observed in images collected by manual. To further explore the clinical practicability of U-HAPPY CT, we enrolled a total of 1186 patients. The scanning results between the two radiologists were highly consistent, regardless of scenarios or pulmonary boundaries (kappa: 0·89−1·00, $P<0·001$; all slope tests for BA plots: $P>0·05$; Fig. S2-5). Although the scanning results under specific semi or manual scenarios varied greatly among hospitals (all, $P<0·01$; Table 2, Fig. S6), when we pooled the results of specific scenarios, we found that, as expected, the full scenario without any human intervention had significantly lower scanning lengths than the others (both, $P<0·001$), while there was no significant difference between the semi and manual scenarios ($P = 0·178$; Fig. 4i, Table 2). Additionally, the scanning length of all four boundaries navigated by U-HAPPY CT was significantly lower than that achieved in the manual scenario (all, $P<0·001$ for the full scenario; all, $P<0·05$ for the semi scenario; Table 2), which indicated the lowest radiation exposure. Except for apex edge ($P>0·15$), which was most likely determined by the distinct and stable bone structure of the pulmonary apex edge, the full scenario presented a significantly smaller edge distance than that of the semi scenario regarding the other three directions, especially for the basis ($P<0·05$ for left and right; $P<0·001$ for basis), which is most susceptible to human interference and respiratory movement. We further calculated the absolute effective dose *mSv* per patient and scaled as $mSv_{\%}$ to eliminate the baseline effect of different scanning protocols. Similar to the scanning length, $mSv_{\%}$ varied significantly among hospitals under specific semi and manual scenarios (both, $P<0·01$), and the full scenario minimized radiation exposure compared to the others (both, $P<0·001$). As expected, manual scanning caused the highest effective dose, even compared to the semi scenario ($P = 0·012$; Fig. 4j, Table 2).

4. Discussion

There is no doubt that we have been thoroughly submerged in the ocean of big data. To swim with this tide, we applied big data principles to the concepts of machine intelligence and deep computing and subsequently concatenated two different convolutional neural networks to empower CT scanner with intelligence to automatically realize an autoplan for chest CT clinical imaging, filling in an essential missing piece in the puzzle of AI-based interventions—the most upstream data collection [15].

In fact, most anatomical pulmonary structures are meaningless but determining the scanning starting point or pulmonary profile is the key for chest CT scanning. Human anatomy determines that the apex of the thoracic cage and the jaw edge of the human face are at approximately the same level, with an interval of only a few cervical vertebra heights. We reason that if the facial lower boundary is determined, then the pulmonary apex boundary can be logically deduced. Therefore, we chose RPN as the core network for facial boundary detection [19], and demonstrated that the model accuracy was almost 100% and the distance error was tolerably within 20 pixels, which satisfied the clinical requirements. To the best of our knowledge, no anecdotes about the hypothesis and application of relevant technologies in the medical field have been reported. Lesion segmentation has been widely studied with satisfactory accuracy assisted by convolutional neural network [20-24]. We applied V-Net to segment

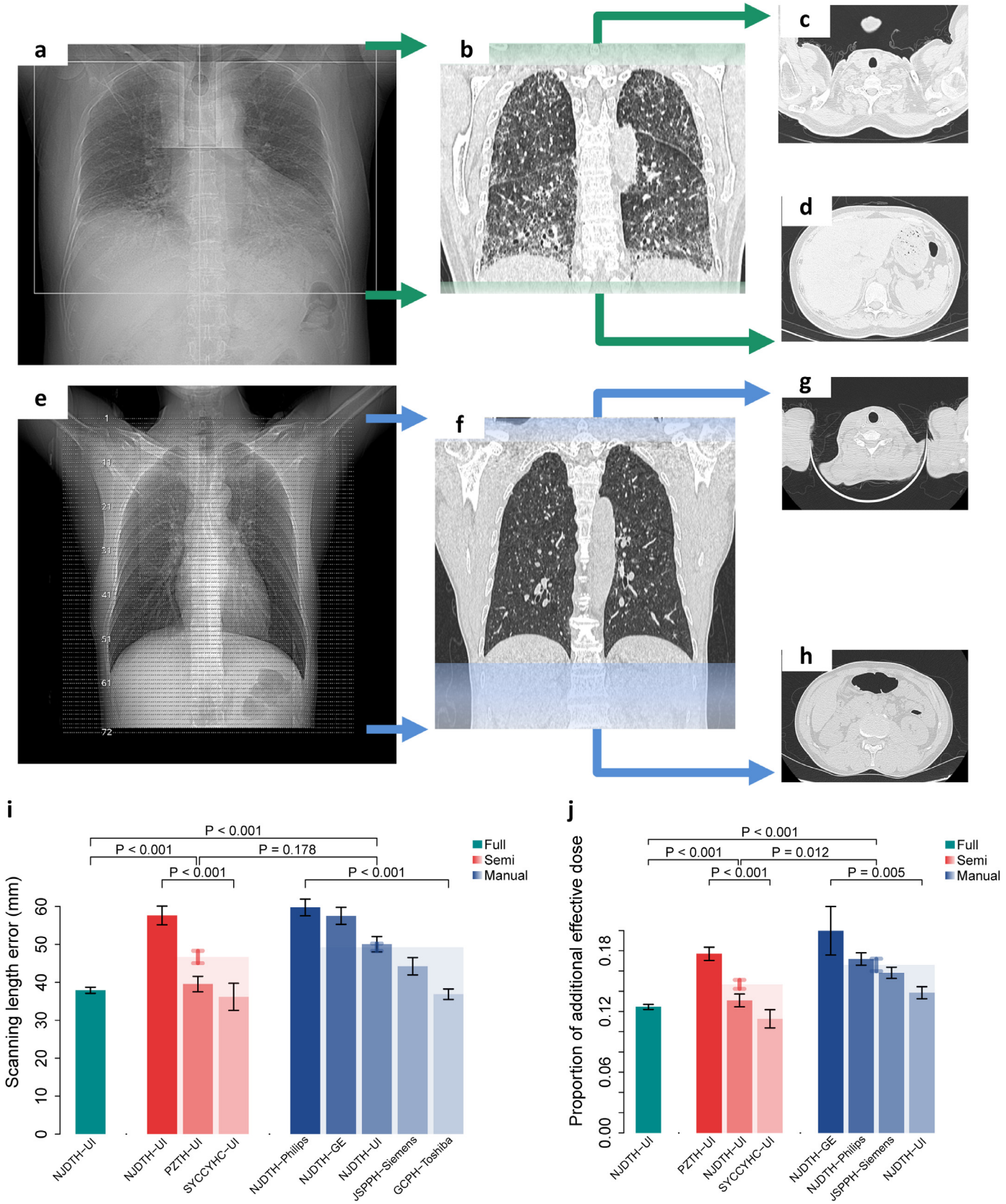

Fig. 4. Practical testing of U-HAPPY CT in three clinical scenarios. a) Image collected by U-HAPPY CT for an ILD patient under full scenario and the corresponding coronal reconstruction images were shown in b) with scanning error (translucent green). Both the top and bottom slices of the collected images were shown in c-d). In contrast, the scanning and image acquisition process of an ILD patient by using GE scanner under manual scenario were shown in e–h) and scanning error was filled by translucent blue. Comparison of the scanning length error and radiation dose among the full, semi and manual scenarios are shown in a) and b), respectively. Bars here present the mean ± standard error of the mean (SEM), and bars with transparent colors were generated by pooling data from multiple hospitals under specific scenarios. Statistical *P*-values were calculated by a two-sample Student's *t*-test or one-way ANOVA for multiple group comparisons. NJDTH: Nanjing Drum Tower Hospital; PZTH: Pizhou Third People's Hospital; SYCCYHC: Chenyang Health Center in the Sheyang District; GCPH: Gaochun People's Hospital.

Table 2
Comparison of scanning efficiency and radiation exposure reduction among three clinical scenarios (n = 1186).

	Clinical Scenario[a,b]			*P*-value[c]		
	Full (F)	Semi (S)	Manual (M)	F vs S	F vs M	S vs M
Number of patients	351	277	558			
Total length error (mm)	37·9 ± 0·8	46·7 ± 1·6 (<0·001)	49·3 ± 1·0 (<0·001)	<0·001	<0·001	0·178
Distance from edge (mm)						
Apex						
Radiologist 1	16·0 ± 0·3	16·6 ± 0·4 (<0·001)	22·6 ± 0·3 (<0·001)	0·273	<0·001	<0·001
Radiologist 2	16·0 ± 0·3	16·7 ± 0·4 (<0·001)	22·7 ± 0·3 (<0·001)	0·185	<0·001	<0·001
Basis						
Radiologist 1	21·9 ± 0·7	30·1 ± 1·5 (<0·001)	26·6 ± 0·9 (<0·001)	<0·001	<0·001	0·047
Radiologist 2	22·1 ± 0·7	30·3 ± 1·5 (<0·001)	26·6 ± 0·9 (<0·001)	<0·001	<0·001	0·037
Left						
Radiologist 1	41·2 ± 0·3	43·3 ± 0·7 (0·003)	48·1 ± 0·7 (<0·001)	0·008	<0·001	<0·001
Radiologist 2	41·1 ± 0·3	42·9 ± 0·7 (0·007)	48·0 ± 0·7 (<0·001)	0·022	<0·001	<0·001
Right						
Radiologist 1	41·0 ± 0·3	43·1 ± 0·7 (0·06)	48·5 ± 0·6 (0·001)	0·005	<0·001	<0·001
Radiologist 2	40·8 ± 0·3	42·9 ± 0·7 (0·055)	48·9 ± 0·6 (0·002)	0·005	<0·001	<0·001
Proportional dose ($mSv_{\%}$)	0·12±0·0	0·15±0·0 (<0·001)	0·17±0·0 (0·005)	<0·001	<0·001	0·012

[a] Values here are presented as the mean ± standard error of the mean (SEM).
[b] One-way ANOVA *P*-value for multiple groups comparison are presented within parenthesis.
[c] Two-sample Student's *t*-test *P*-value.

the pulmonary area on the topograms and determined the boundaries of lung tissues, and the scanning field obtained by V-Net was more accurate than the manual scenario.

The subjects observed from the camera follow the law of 'perspective effect' (i.e., objects appear smaller when farther away and present natural anomalies). To simplify this problem, we adopted a concise calibration method to synchronize the camera and CT scanning couch instead of the relatively classic 'standard chess correction method' (chess for short) because of its costly requirements for hardware and software adaptation [25]. As a rough estimate, the additional cost would be only an ordinary camera and our calibration method cost only 1/5 compared to a 3-dimensional camera. Notably, the 2-dimensional camera covered the problem of side correction by fixing the couch height; such approach reduces the accuracy of lateral orientation [25], but the computational complexity is lower than that of 3-dimensional cameras, resulting in a reduction in data volume and time consumption.

Practically, the accuracy of the scanning length was directly related to radiation dose exposure, such that fully applying U-HAPPY CT potentially reduces additional radiation exposure, which is friendly and feasible for patients with diseases that required repeated follow-up (e.g., ILD). Interestingly, we found significant differences in scanning accuracy and effective radiation dose among different hospitals. Contrary to common sense, lower-ranking hospitals seemed to have better control over the scanning region than higher-ranking hospitals, which might be because the number of receptions in lower-ranking hospitals is far less than that of superior hospitals, leading to delicate operations in scanning; such phenomenon could also be affected by China's healthcare policy and tremendous population base.

Due to the new concept of intelligent CT, including automatic recognition, planbox, positioning, and a more user-friendly interface, U-HAPPY CT is expected to cover almost the entire upstream of imaging workflow because of the ability to save the radiographers' judgement and manual processes; other streamlined operations have not been completely eliminated, mainly because of legal and regulatory restrictions. Such rules consider that the operation accuracy requires manual judgement; thus, some control keys were installed on only the scanning gantry of the CT machines (e.g., GE), and some machines retained direction keys on the control keyboard in other rooms (*e.g.*, Philips). Although the success rate in the current experiment was 100%, in case of an incomplete lung scan, the radiographers can still select the manual operation button to continue scanning the incomplete pulmonary tissue.

However, some limitations should be noted. First, all adults in the training and testing datasets involved in V-Net construction were Chinese, and no other races were enrolled. The lack of adolescents, infants and multi-ethnic patients may bias the model performance toward the size selection of planbox during scanning. Second, we didn't include all the patient positions on the scanning couch in the automatic scanning mode, such as feet-first, prone position, lateral position and other special conditions. Third, a certain degree of lower jaw angle is totally tolerable for facial detection by U-HAPPY CT, but some extreme angles are not considered especially for those unconscious patients who were admitted to the emergency department; such patients are recommended to be scanned fully by manual under the care of a doctor.

Briefly, a concatenation of two deep convolutional neural networks and classic pattern recognition were introduced to perfect the upstream of the imaging workflow. The system used AI to control machines to automatically acquire images and showed promise for facilitating detection and segmentation of the human chest. We believe that establishing the new generation's intelligent CT will complete the last puzzle piece in combining AI and medical imaging.

Data sharing

The data, including original images of pulmonary segmentation and other relevant resources, code and partial modeling results that support the findings of this study are openly available in PanBaiDu at https://pan.baidu.com/s/1tNpchJVUKGQGjLR8k-Iw1g. To protect patient privacy, all data involved in the testing set for facial detection are not accessible and were not stored on local servers for long periods.

Declaration of Competing Interest

The authors declare no competing interests.

Acknowledgments

We would like to thank two experts (Chunfeng Qian, 17 years of experience; Xiaoming Wu, 11 years of experience) who provided us with great help in image labeling. In addition, we would like to express our considerable gratitude to United Imaging (Shanghai, China), who provided technology support and graphics processing units for this work. This work was supported by the National Natural Science Foundation of China (81720108022, 91649116, 81571040,

81973145), the Social Development Project of Science and Technology in Jiangsu Province (BE2016605, BE201707), the National Key R&D Program of China (2017YFC0112801), the Key Medical Talents of Jiangsu Province, the '13th Five-Year' Health Promotion Project of Jiangsu Province (B.Z.2016-2020), the Jiangsu Provincial Key Medical Discipline (Laboratory) (ZDXKA2016020), the Project of the Sixth Peak of Talented People (WSN-138, BZ), the China Postdoctoral Science Foundation (2019M651805), the "Double First-Class" University project (CPU2018GY09). The funders had no role in study design, data collection, data analysis, interpretation, or writing of the report.

Supplementary materials

Supplementary material associated with this article can be found in the online version at doi:10.1016/j.ebiom.2020.102724.

References

[1] Wells A, Hirani N. Interstitial lung disease guideline. Thorax 2008;63(Suppl 5): v1–v58.
[2] Power SP, Moloney F, Twomey M, James K, O'Connor OJ, Maher MM. Computed tomography and patient risk: facts, perceptions and uncertainties. World J Radiol 2016;8(12):902–15.
[3] Hsieh J. Computed tomography: principles, design, artifacts, and recent advances. Bellingham, WA: SPIE; 2009.
[4] National Lung Screening Trial Research Team, Aberle D, Adams A, Berg C, Black W, Clapp J, et al. Reduced lung-cancer mortality with low-dose computed tomographic screening. N Engl J Med 2011;365(5):395–409.
[5] Aberle DR, DeMello S, Berg CD, Black WC, Brewer B, Church TR, et al. Results of the two incidence screenings in the national lung screening trial. N Engl J Med 2013;369(10):920–31.
[6] Kalra MK, Maher MM, Toth TL, Hamberg LM, Blake MA, Shepard J-A, et al. Strategies for CT radiation dose optimization. Radiology 2004;230(3):619–28.
[7] Brenner DJ, Hall EJ. Computed tomography—an increasing source of radiation exposure. N Engl J Med 2007;357(22):2277–84.
[8] Goldman LW. Principles of CT: radiation dose and image quality. J Nucl Med Tech 2007;35(4):213–25.
[9] Kalra MK, Sodickson AD, Mayo-Smith WW. CT radiation: key concepts for gentle and wise use. Radiographics 2015;35(6):1706–21.
[10] Ting DS, Liu Y, Burlina P, Xu X, Bressler NM, Wong TY. AI for medical imaging goes deep. Nat Med 2018;24(5):539–40.
[11] Wang F, Casalino LP, Khullar D. Deep learning in medicine—promise, progress, and challenges. JAMA Intern Med 2019;179(3):293–4.
[12] Liang H, Tsui BY, Ni H, Valentim CCS, Baxter SL, Liu G, et al. Evaluation and accurate diagnoses of pediatric diseases using artificial intelligence. Nat Med 2019;25 (3):433–8.
[13] Wang Y, Yan F, Lu X, Zheng G, Zhang X, Wang C, et al. IILS: intelligent imaging layout system for automatic imaging report standardization and intra-interdisciplinary clinical workflow optimization. EBioMedicine 2019;44:162–81.
[14] Lakhani P, Sundaram B. Deep learning at chest radiography: automated classification of pulmonary tuberculosis by using convolutional neural networks. Radiology 2017;284(2):574–82.
[15] Bi WL, Hosny A, Schabath MB, Giger ML, Birkbak NJ, Mehrtash A, et al. Artificial intelligence in cancer imaging: clinical challenges and applications. CA Cancer J Clin 2019;69(2):127–57.
[16] Long J, Shelhamer E, Darrell T. Fully convolutional networks for semantic segmentation. IEEE Trans Pattern Anal Mach Intell 2014;39(4):640–51.
[17] Christner JA, Kofler JM, McCollough CH. Estimating effective dose for CT using dose–length product compared with using organ doses: consequences of adopting international commission on radiological protection publication 103 or dual-energy scanning. Am J Roentgenol 2010;194(4):881–9.
[18] International Electrotechnical Commission. Medical electrical equipment—part 2-44: particular requirements for the basic safety and essential performance of X-ray equipment for computed tomography. International Electrotechnical Commission (IEC); 2010. p. 60601-2-44.
[19] Ren S, He K, Girshick R, Sun J. Faster R-CNN: towards real-time object detection with region proposal networks. IEEE Trans Pattern Anal Mach Intell 2017;39 (6):1137–49.
[20] Heo S-J, Kim Y, Yun S, Lim S-S, Kim J, Nam C-M, et al. Deep learning algorithms with demographic information help to detect tuberculosis in chest radiographs in annual workers' health examination data. Int J Environ Res Public Health 2019;16 (2):E250.
[21] Kamnitsas K, Ledig C, Newcombe VF, Simpson JP, Kane AD, Menon DK, et al. Efficient multi-scale 3D CNN with fully connected CRF for accurate brain lesion segmentation. Med Image Anal 2017;36:61–78.
[22] Greenspan H, Van Ginneken B, Summers RM. Guest editorial deep learning in medical imaging: overview and future promise of an exciting new technique. IEEE Trans Med Imaging 2016;35(5):1153–9.
[23] Litjens G, Kooi T, Bejnordi BE, Setio AAA, Ciompi F, Ghafoorian M, et al. A survey on deep learning in medical image analysis. Med Image Anal 2017;42:60–88.
[24] Sirinukunwattana K, Raza SEA, Tsang Y, Snead DRJ, Cree IA, Rajpoot NM. Locality sensitive deep learning for detection and classification of nuclei in routine colon cancer histology images. IEEE Trans Med Imaging 2016;35(5):1196–206.
[25] Zhang Z. A flexible new technique for camera calibration. IEEE Trans Pattern Anal Mach Intell 2000;22(11):1330–4.